INTERNATIONAL JOURNAL OF HYDROGEN ENERGY 48 (2023) 9620–9635

Available online at www.sciencedirect.com

ScienceDirect

journal homepage: www.elsevier.com/locate/he

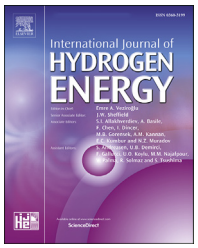

V_2O_5 nanoribbons/N-deficient g-C_3N_4 heterostructure for enhanced visible-light photocatalytic performance

Ahmed E. Hassan [a,b,c], *Mohamed Hammad Elsayed* [c,d], *Mai S.A. Hussien* [e,f], *Mohamed Gamal Mohamed* [g,h], *Shiao-Wei Kuo* [g], *Ho-Hsiu Chou* [d], *Ibrahim S. Yahia* [i,j,k,***], *Tarek A. Mohamed* [c,**], *Zhenhai Wen* [a,*]

[a] *CAS Key Laboratory of Design and Assembly of Functional Nanostructures, And Fujian Provincial Key Laboratory of Materials and Techniques Toward Hydrogen Energy, Fujian Institute of Research on the Structure of Matter, Chinese Academy of Sciences, Fuzhou, Fujian, 350002, China*

[b] *University of Chinese Academy of Sciences, Beijing, 100049, China*

[c] *Department of Chemistry, Faculty of Science, Al-Azhar University, Nasr City 11884, Cairo, Egypt*

[d] *Department of Chemical Engineering, National Tsing Hua University, Hsinchu, 30013, Taiwan*

[e] *Department of Chemistry, Faculty of Education, Ain Shams University, Roxy, Cairo 11757, Egypt*

[f] *Nanoscience Laboratory for Environmental and Bio-medical Applications (NLEBA), Department of Physics, Faculty of Education, Ain Shams University, Roxy, Cairo 11757, Egypt*

[g] *Department of Materials and Optoelectronic Science, Center of Crystal Research, National Sun Yat-Sen University, Kaohsiung 80424, Taiwan*

[h] *Chemistry Department, Faculty of Science, Assiut University, Assiut 71516, Egypt*

[i] *Research Center for Advanced Materials Science (RCAMS), King Khalid University, Abha 61413, P.O. Box 9004, Saudi Arabia*

[j] *Advanced Functional Materials & Optoelectronic Laboratory (AFMOL), Department of Physics, Faculty of Science, King Khalid University, P.O. Box 9004, Abha, Saudi Arabia*

[k] *Semiconductor Lab., Department of Physics, Faculty of Education, Ain Shams University, Roxy, 11757 Cairo, Egypt*

* *Corresponding author*. CAS Key Laboratory of Design and Assembly of Functional Nanostructures, and Fujian Provincial Key Laboratory of Materials and Techniques toward Hydrogen Energy, Fujian Institute of Research on the Structure of Matter, Chinese Academy of Sciences, Fuzhou, Fujian, 350002, China.

** *Corresponding author*.

*** *Corresponding author*.

E-mail addresses: ihussein@kku.edu.sa (I.S. Yahia), tarek_ama@azhar.edu.eg (T.A. Mohamed), wen@fjirsm.ac.cn (Z. Wen).

https://doi.org/10.1016/j.ijhydene.2022.12.009

HIGHLIGHTS

- V_2O_5 nanoribbons/N-deficient g-C_3N_4 was synthesized as S-scheme heterojunction photocatalyst.
- The photocatalyst showed high visible-light photocatalytic activity for H_2 production and pollutants degradation.
- The photocatalyst exhibited excellent stability.
- The photocatalytic mechanism was studied based on the experimental and DFT calculations.

GRAPHICAL ABSTRACT

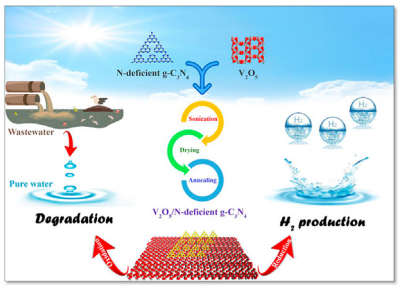

ARTICLE INFO

Article history:
Received 25 August 2022
Received in revised form
9 November 2022
Accepted 1 December 2022
Available online 27 December 2022

Keywords:
H_2 evolution
Photodegradation
V_2O_5/N-deficient g-C_3N_4
S-scheme heterojunction
DFT

ABSTRACT

Visible-light-induced heterostructure photocatalysts have been regarded as promising candidates in clean energy production and environmental treatment of organic pollutants. In this study, we have prepared nanocomposites of V_2O_5/N-deficient g-C_3N_4 (VO/Ndef-CN), which have been characterized by a variety of techniques. The as-synthesized nanocomposites show efficient bifunctional photocatalytic properties toward hydrogen generation and pollutants degradation (dye and antibiotic). The optimized 5VO/Ndef-CN photocatalyst exhibits improved photoactivity for H_2 production (5892 μmol g^{-1} h^{-1}), with a high quantum yield of 6.5%, and fast degradation of organic pollutants, as well as high photocatalytic stability under visible light irradiation. The high photocatalytic efficiency is due to the presence of N defects and S-scheme heterojunction formation, which leads to rapid charge separation, enhanced visible-light absorption, and increased active sites. Furthermore, the possible activity-enhanced mechanism and the photodegradation pathway are proposed based on the experimental and density functional theory (DFT) investigations.

Introduction

Recent years have seen the emergence of challenges such as the energy crisis and environmental deterioration that have attracted the widespread attention of scientists [1,2]. Hydrogen fuel has received significant interest as a renewable, clean, and promising substitute energy source for fossil fuels. On the other hand, pollutants such as antibiotics and dyes are harmful to the environment in addition to human health, even in trace amounts [3,4]. Photocatalysis has been demonstrated to be a viable technique that can be employed for H_2 generation, CO_2 reduction, pollutant degradation, disinfection, organic transformation, etc., and it has emerged as a powerful solution for addressing environmental and energy issues [5–12]. However, their economic applicability is restricted due to low visible-light utilization [2,13]. As a result, many efforts have been devoted to resolving these issues and developing practical and economic applications. Among the reported photocatalysts is g-C_3N_4, a new class of polymeric semiconductors that was highlighted as a potential candidate for H2 generation and pollutant degradation [14–21] due to its reasonable cost, appropriate bandgap (2.7 eV), large surface area, and excellent stability. Nevertheless, its photocatalytic efficiency is severely constrained by the rapid recombination of electron-hole (e^--h^+) pairs and insufficient sunlight absorption [22–24]. Numerous techniques have been developed to address these issues and enhance the photocatalytic performance of g-C_3N_4, including morphology control [25,26], element doping [14,27,28], copolymerization [29,30], the introduction of vacancy defects [31,32], and the construction of a heterojunction [33–35].

The heterojunction formation is one of the most efficient and appropriate strategies known for increasing the efficiency of g-C_3N_4. According to the bandgap's relative positions, there are many types of heterojunctions. For example, there are type-I, type-II, p-n, Z-scheme, and S-scheme heterojunctions [36–38], among which Z-scheme, in comparison with the traditional heterojunction, can effectively promote e^--h^+ separation in different semiconductors [36]. However, photogenerated charge transfer, weak redox abilities of charge carriers, and poor light absorption were identified in this system, impeding the enhancement of photocatalytic performance [39,40]. Recently, the step-scheme (S-scheme) heterojunction has been developed to overcome the thermodynamics, kinetics, and energy problems of type-II,

conventional, and all-solid-state Z-scheme heterojunctions [19,21,39–41]. The S-scheme heterojunction consists of an oxidizing and a reducing photocatalyst. When the two photocatalysts with staggered band structures contact, their Fermi levels stay at the same level, resulting in band bending. This band bending separates photogenerated carriers and decreases their recombination [21,41]. Finally, the strong photoinduced e^- and h^+ are retained in the conduction band (CB) of the reduction photocatalyst and the valence band (VB) of the oxidation photocatalyst, whereas the weak photogenerated charge carriers are recombined. Overall, the S-scheme heterojunction system enables charge separation and exhibits excellent redox ability, resulting in enhanced photocatalytic performance. Therefore, S-scheme heterojunction seems to be an excellent option for photocatalysis. The key to fabricating an S-scheme heterojunction is identifying a semiconductor with an appropriate band structure and Fermi level for g-C_3N_4. We have chosen V_2O_5 as another component of the photocatalyst, which is a layered semiconductor with several advantages, including a narrow bandgap (~2.3 eV), a broad response spectrum to light, relative chemical stability, and high oxidation ability [35,42]. Furthermore, V_2O_5 possesses appropriate band edges, which may combine effectively with g-C_3N_4 to form an S-scheme heterostructure [4,34]. Researchers have recently reported a V_2O_5/g-C_3N_4 heterostructure with enhanced photocatalytic efficiency. Preeyanghaa et al. reported that the S-scheme rod-like g-C_3N_4/V_2O_5 heterostructure improves the tetracycline antibiotic degradation performance [34]. In addition, as reported by Le et al., the V_2O_5-g-C_3N_4 S-scheme nanocomposite displayed a high removal efficiency for amoxicillin under solar light [4]. Zhang et al. developed a V_2O_5/P-g-C_3N_4 composite via heat treatment and found that it exhibited higher methyl orange removal efficiency than pure V_2O_5 and P-g-C_3N_4 [35]. Oliveros et al. demonstrated photocatalytic diclofenac removal by V_2O_5/B-g-C_3N_4 composite, and the efficiency reached ~100% [43]. Dadigala et al. reported that V_2O_5 nanorods/g-C_3N_4 exhibited high photoreduction efficiency for Cr (VI) and photodegradation for congo red dye [3]. All reports indicate that heterojunction which promotes charge separation in the photocatalytic process enhances photocatalytic efficiency over the separate use of pure V_2O_5 and g-C_3N_4. However, research on the V_2O_5/g-C_3N_4 heterostructure has been limited to the degradation of the pollutants. On the other hand, the presence of nitrogen defects in g-C_3N_4 has recently been discovered to be advantageous in photocatalytic processes [44–47]. Defects can adjust the electronic states of the material and are likely to behave as active sites for reactive species, thus enhancing the photocatalytic activity. Therefore, it is expected that the combining of the two advantageous features (introducing N defects into the g-C_3N_4 matrix and forming S-scheme heterojunction) will be extremely effective in achieving superior photocatalytic performance in energy production and environmental remediation. To the best of our knowledge, no work has yet demonstrated the photocatalytic activity of the V_2O_5/N deficient g-C_3N_4 heterostructure for both H_2 generation and degradation of hazardous pollutants such as amoxicillin and indigo carmine dye.

In this study, following the hypothesis mentioned earlier, we successfully constructed a novel V_2O_5/N-deficient g-C_3N_4 heterojunction (donated as VO/Ndef-CN). For preparing a new heterojunction composite, the N defect was introduced into g-C_3N_4 through urea ($CO(NH_2)_2$) and formamide ($HCONH_2$) copolymerization. The resultant product (N-deficient g-C_3N_4) was then combined with V_2O_5 using a facile solvothermal-calcination method to synthesize the S-scheme heterojunction composites. The prepared samples were examined by different characterization techniques, and their photocatalytic activities toward hydrogen production and pollutant degradation were evaluated. The formed S-scheme heterojunction photocatalyst may improve the contact region between V_2O_5 and N-deficient g-C_3N_4 and enhance the charge carrier's separation, thus promoting photocatalytic performance. In comparison to V_2O_5 and g-C_3N_4, the VO/Ndef-CN composites displayed a broader visible-light absorption and superior photocatalytic activity for hydrogen generation and photodegradation of amoxicillin (AMOX) and indigo carmine (IC). Additionally, the 5VO/Ndef-CN composite displayed the optimum photocatalytic efficiency and possessed high stability. Furthermore, the suggested photocatalytic mechanisms for improved photocatalytic activity have been explored by coupling the experimental methods with density functional theory (DFT) calculations. This study sheds light on the fabrication of V_2O_5/N-deficient g-C_3N_4 heterojunction photocatalysts with enhanced performance.

Experimental section

Materials

All chemicals and solvents were analytical grade and used as received without further purification. Distilled water was used in all experiments. Urea (99.0%, Chem-Lab), formamide (99.5%, Sigma Aldrich), ammonium vanadate (99.0%, SDFCL), citric acid monohydrate (99.5%, Sigma Aldrich), methanol (99.9%, VWR Chemicals), amoxicillin trihydrate (99.9%, Gamma laboratory chemicals), indigo carmine (dye content >85.0%, SDFCL), isopropanol (99.0%, ALPHA CHEMIKA), ethylenediaminetetraacetic acid (98.0%, ADWIC), *p*-benzoquinone (98.0%, Loba Chemie), triethanolamine (99.0%, Sigma Aldrich), tetrahydrofuran (99.5%, Sigma Aldrich), sodium sulfate (99.0%, Sigma Aldrich).

Synthesis of photocatalysts

First, N-deficient g-C_3N_4 (Ndef-CN) was fabricated by copolymerization of urea and formamide [47]. Urea (10.0 g) and formamide (0.1 mL) were homogeneously mixed, subsequently heated to 550 °C in a muffle furnace for 2 h at a rate of 5 °C/min, and finally allowed to cool to 25 °C. For comparison, pure g-C_3N_4 (CN) was synthesized under the same conditions through direct calcination of urea. Then, V_2O_5 (VO) was formed by mixing ammonium vanadate and citric acid (1:3 mol ratio) and stirring the resulting solution to achieve homogeneity. Following that, the solution was heated to 80 °C to get a vanadium-citrate precursor that was calcined for 3 h at 450 °C to obtain V_2O_5. The VO/Ndef-CN nanocomposites were synthesized according to the procedure shown in Scheme 1 by dissolving 0.1 g of Ndef-CN and different

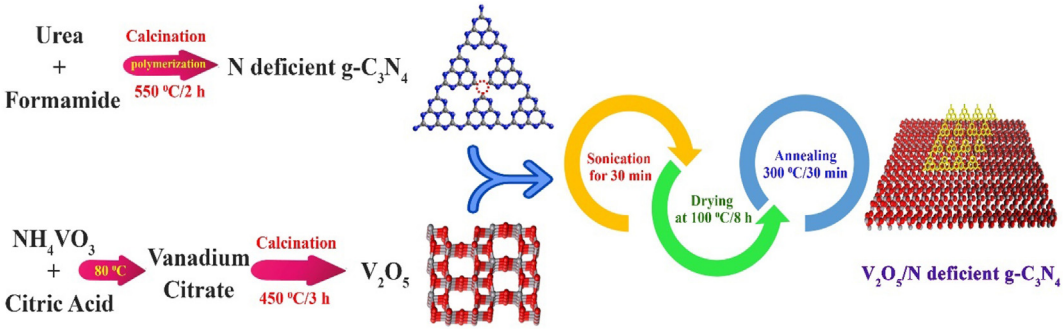

Scheme 1 – Synthesis schematic illustration of xVO/Ndef-CN nanocomposites.

amounts of VO (5, 10, and 25 wt%) in methanol, followed by sonication and drying at 80 °C for 8 h. After evaporating the methanol, the V_2O_5/Ndef-CN was annealed at 300 °C for 30 min in a muffle furnace and then ground into a homogenous powder. The obtained VO/Ndef-CN heterojunctions with different VO mass contents were donated as *x*VO/Ndef-CN (x = 5, 10, and 25 wt%).

Characterization

X-ray diffraction (XRD) was used to investigate the crystal structures of the prepared photocatalysts using the X'Pert Pro diffractometer and Cu Kα radiation (λ = 1.5406 Å) in the 2θ range from 5° to 80°. Fourier transform infrared (FT-IR) spectra were acquired using a Bruker Tensor-27 FT-IR spectrophotometer with a resolution of 4 cm^{-1}. X-ray photoelectron spectroscopy (XPS) was performed on the ULVAC-PHI PHI 5000 Versaprobe II chemical analysis electron spectrometer (ESCA). Thermogravimetric analysis (TGA) was recorded under N_2 using a TGA Q-50 analyzer from 40 to 800 °C and a heating rate of 20 °C min^{-1}. Transmission electron microscopy (TEM) images were acquired at 200 kV using a JEOL 2100 instrument. The scanning electron microscope (SEM, JEOL JSM-6500) was used to examine the morphology of the materials. Photoluminescence (PL) spectra were captured using a Hitachi F-7000 fluorescence spectrophotometer with an excitation wavelength of 370 nm. The bandgap energies (E_g) were determined using the UV–Vis diffused reflectance spectra (UV–Vis DRS) recorded using a Hitachi U-3300 spectrophotometer with $BaSO_4$ as the background. The percentage of vanadium incorporated in the prepared samples was determined using the iCAP 7000 Series ICP spectrometer. The Brunauer-Emmett-Teller (BET) technique was used to calculate the specific surface area (SSA) by examining N_2 isotherms at 77 K using Micromeritics ASAP 2020.

Photocatalytic experiments

Hydrogen generation

Experiments on H_2 generation were conducted at room temperature in a 35 mL Pyrex photoreactor connected to a closed gas circulation and evacuation system (Fig. S1a). During this process, the prepared photocatalyst (1.5 mg) was suspended in an aqueous solution, including triethanolamine (TEOA; 10 vol %) as a sacrificial agent and a co-catalyst of Pt (5 wt%). Before light irradiation, intensive ultrasonic processing was followed by Ar bubbling to degas the resulting mixture. The suspension was irradiated under a simulated sunlight environment by 1000 W/m^2 (1 sun) radiation at $\lambda > 420$ nm. The evolved H_2 was analyzed using a gas chromatograph (Shimadzu, GC-2014), while Ar served as the carrier gas in this study. A thermal conductivity detector was used to detect hydrogen by comparing it to standard hydrogen gases with specified concentrations. For 5VO/Ndef-CN hydrogen generation, the apparent quantum yields (AQY) were calculated as follows:

$$AQY = \frac{2 \times Number\ of\ evolverd\ H_2\ molecules}{Number\ of\ incedient\ photon} \times 100\% = \frac{2 \times M \times N_A}{S \times P \times t \times \frac{\lambda}{(h \times c)}} \times 100\%$$

Where M is the H_2 evolution amount; N_A is the Avogadro constant; S is the irradiation area; P is the incident light intensity (W/m^2); t is the time of light irradiation; λ is the wavelength of monochromatic light; h is the Planck constant; c is light velocity. For the AQYs measurement, the mixed solutions consisted of a photocatalyst (x mg/mL water) and a sacrificial agent; and were illuminated with the light source of a Xenon lamp (AM1.5) with a particular wavelength filter.

Pollutants degradation

The photocatalytic activities of the prepared samples were investigated by AMOX (antibiotic) and IC (dye) photodegradation. The photodegradation of pollutants in the presence of photocatalyst was carried out in a homemade photoreactor (100 × 65 cm), in which a connected air fan circulates the air within the system to avoid a thermal effect in the photocatalytic reaction process, and the light source (LED lamps with a power of 18 W) was installed 5 cm above the samples (Fig. S1b). Firstly, the photocatalyst (5 mg) was added to 25 mL of IC (20 ppm) or AMOX (25 ppm). The adsorption-desorption equilibrium was achieved after 30 min of stirring in the dark. After that, the suspensions were illuminated with 18 W LED lamps as a visible light source. At given time intervals, about 3 mL of aliquots were centrifuged to remove the photocatalyst particles. Finally, the UV–Vis. spectrophotometer measured pollutant concentrations, and the λ_{max} decreased with time (λ_{max} of IC and AMOX are 612 and 230 nm, respectively). To find the optimal *x*VO/Ndef-CN photocatalyst

composition, we investigated the photocatalytic response of these dye and antibiotic solutions. Additionally, five-cycle stability tests were performed to assess photocatalytic stability.

The photodegradation efficiency was calculated using the following mathematical formula:

$$Degradation\ (\%) = \frac{C_\circ - C}{C_\circ} \times 100\ \%$$

Where C_0 and C are the initial and final concentrations of the pollutants, respectively.

Computational studies

The first-principles calculations were performed with the help of the DFT incorporated in the Materials Studio DMol3 code [48]. Fukui Functions describing radical (f^0), nucleophilic (f^-), and electrophilic attack (f^+) were used to predict the possible reaction sites of the organic pollutants and the photodegradation pathway. Furthermore, the band structure (BS) and density of states (DOS) were used to describe the electronic properties of the optimized structures of N-deficient g-C_3N_4 and V_2O_5 with 5 × 5 × 1 K-points. The B3LYP [49,50] and GGA-PBE functionals [51] were considered to describe the Fukui Function and electronic properties, respectively, with the double numerical basis set (DNP) and the DFT Semi-core Pseudopots. The self-consistent field (SCF) convergence was adjusted to 10^{-6} Ha, and the smearing changed to 0.005 Ha. The maximum displacements and force were 5 × 10^{-3} Å and 2 × 10^{-3} Ha/Å, respectively, whereas the energy of the system was converged to 10^{-5} Ha. The van der Waals interactions were described using the DFT-D correction of Grimme.

Results and discussion

Characterizations

XRD analysis

Fig. 1a exhibits XRD patterns of VO, CN, Ndef-CN, and *x*VO/Ndef-CN nanocomposites. The XRD of CN and Ndef-CN reveals a significant degree of structural similarity. Both samples exhibit two distinctive peaks at 2θ of 27.4° and 13.5°, corresponding to the (002) and (100) planes, respectively, which correlate to the aromatic system's interplanar stacking peaks and characteristic *in-plane* structural packing (JCPDS no. 87–1526) [47,52]. However, the Ndef-CN showed a minor shift to lower angles due to the inclusion of formamide, suggesting that the interplanar distance between the graphitic layers increased, which assisted reactant molecules in accessing the interplanar region, hence improving the photocatalytic process [47]. The observed peaks in the VO pattern are found consistent with the V_2O_5 orthorhombic structure (JCPDS no. 03–0207) [43]. Nevertheless, the hexagonal phase of Ndef-CN and the orthorhombic phase of VO can be observed in the *x*VO/Ndef-CN composite. According to the results of the XRD investigation, the photocatalysts are two-phase hybrids with no new phase development. It is believed that the contact between VO and Ndef-CN occurs through strong electrostatic interactions [43]. Furthermore, the VO peak intensity increases with increasing VO loading in the composite, whereas the peak intensity of Ndef-CN decreases [53,54].

FT-IR analysis

The FT-IR spectra of VO, CN, Ndef-CN, and *x*VO/Ndef-CN photocatalysts are displayed in Fig. 1b. For CN, the vibration mode of N–H stretching is ascribed to the characteristic bands between 3100 and 3500 cm^{-1} [53,55]. The C=N and C–N heterocycles stretches were detected in the 1650–1240 cm^{-1} region [56]. The s-triazine rings breathing mode is observed at 809 cm^{-1} [43,56]. When the FT-IR spectrum of CN is compared to Ndef-CN, the characteristic absorbance of CN remains almost unchanged, suggesting that the addition of formamide did not significantly change the CN's fundamental chemical skeleton [47]. For V_2O_5, the vibrations of the V–O–V bond asymmetric stretch and the V=O bond stretch have been attributed to the observed IR bands at 824 and 1014 cm^{-1}, respectively [43,53]. The *x*VO/Ndef-CN heterostructure FT-IR spectra show the overlap between the VO and Ndef-CN spectra. With increasing the V_2O_5 content, the peak intensity of Ndef-CN decreases. This result reveals that VO and Ndef-CN coexist in the nanocomposite [53]. All the characteristic peaks of both VO and Ndef-CN can be found in the VO/Ndef-CN heterojunction, indicating the successful formation of VO/Ndef-CN photocatalysts.

TGA analysis

Thermogravimetric analysis of VO, CN, Ndef-CN, and *x*VO/Ndef-CN composites are shown in Fig. 1c. As can be observed, VO loses insignificant weight due to the high boiling point (1750 °C), while other samples exhibit a noticeable mass loss in the range of 500–750 °C. Pure-CN is relatively stable below 500 °C, and it is wholly decomposed at about 710 °C [57]. The thermal stability of CN significantly decreases upon loading VO onto it [42]. This work hypothesizes that V_2O_5 acts as a catalyst capable of absorbing and activating O_2 in the air and subsequently oxidizing the g-C_3N_4 at a relatively low temperature [56]. The weight loss of graphitic carbon nitride-based materials is mostly due to g-C_3N_4 thermal decomposition, while the remaining residue is related to the V_2O_5 content. The actual mass ratio of V_2O_5 in the nanocomposites was found to be 4.7%, 10.3%, and 25.2% for 5VO/Ndef-CN, 10VO/Ndef-CN, and 25VO/Ndef-CN, respectively. These findings, which are pretty close to the experimentally added contents (5, 10, and 25%), are also shown in Table S1.

Surface area and pore size estimation

Fig. 1d shows the BET-specific surface areas (S_{BET}) and the pore size distribution (PSD) curves of Ndef-CN and *x*VO/Ndef-CN. All samples exhibited type IV isotherms for N_2 adsorption-desorption, confirming the presence of mesoporous structures [35,43]. Compared with Ndef-CN (S_{BET} = 32.83 m^2/g), the 5VO/Ndef-CN sample had a higher surface area (S_{BET} = 36.52 m^2/g), resulting from the porous morphology caused by the copolymerization of urea and formamide. Thus, 5VO/Ndef-CN possessed additional active sites, favoring efficient photocatalytic reactions. As the VO content increased, the S_{BET} of *x*VO/Ndef-CN photocatalysts decreased (Table S1). This is because of the higher VO particle coverage, inhibiting N_2 probe molecules from entering. The pore volume study

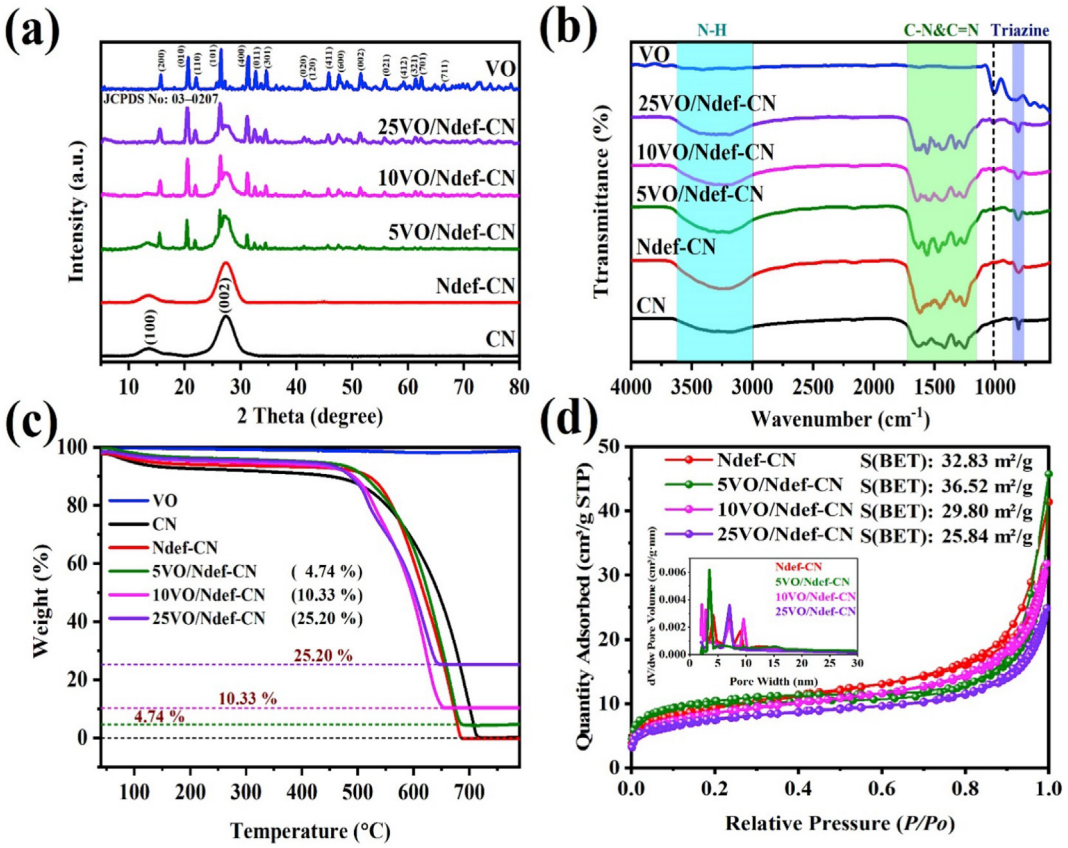

Fig. 1 – (a) XRD patterns, (b) FT-IR spectra, and (c) TGA curves of pure CN, Ndef-CN, VO, and *x*VO/Ndef-CN samples. (c) BET and PSD curves of Ndef-CN and *x*VO/Ndef-CN samples.

confirms that the excessive amount of VO blocks the Ndef-CN channels and pores [43]. The textural properties are summarized in Table S1. The PSD curves demonstrate a pore diameters range between 2 and 13 nm in all photocatalysts (inset of Fig. 1d (left)), suggesting a well-developed mesoporous structure in the nanocomposite [54]. The 5VO/Ndef-CN displays a larger pore volume than the Ndef-CN, showing that the surface properties of the nanocomposite have been significantly influenced.

XPS studies

To further investigate the chemical composition of CN, Ndef-CN, and *x*VO/Ndef-CN, XPS analysis was carried out. The survey spectra (Fig. 2a) indicate that carbon, nitrogen, and oxygen were detected on the surface of CN as well as Ndef-CN; similarly, carbon, nitrogen, vanadium, and oxygen were also found on the surface of the *x*VO/Ndef-CN nanocomposite. The elemental composition in the atomic percentage of the prepared samples was summarized in Table S2. It was found that the elemental composition of vanadium and oxygen increases as the content of V_2O_5 increases in the nanocomposite (Fig. 2a and Table S2). The optimal photocatalyst (5VO/Ndef-CN) composition was quantified as being 45.22% of C, 47.40% of N, 6.82% of O, and 0.56% of V. Furthermore, the percentage of vanadium incorporated in the prepared samples was determined using the ICP technique. The result indicates that the V % were 2.92%, 6.37%, and 12.73% for 5VO/Ndef-CN, 10VO/Ndef-CN, and 25VO/Ndef-CN, respectively (Table S3). This result proved the presence of the V inside the crystal structure of the prepared samples. To explore the impact of formamide inclusion on CN's chemical skeleton, the high-resolution XPS surface analysis of CN and Ndef-CN was conducted. The C 1s (Fig. S2a) and N 1s (Fig. S2b) spectra of both samples display similar peak shapes, with the binding energy shifting slightly to higher energy as a result of N defects with additional redistributed electrons following the introduction of $HCONH_2$ into g-C_3N_4 [47]. The area ratio of N═C-$(N)_2$/C–C in the Ndef-CN sample is higher than pure-CN (Table S4). Additionally, Table S5 and Fig. S2 show that the ratio of peak area between C═N–C and N-$(C)_3$ significantly increases from 2.04 of pure-CN to 4.04 of Ndef-CN, indicating that nitrogen deficiency is mainly located in the N-$(C)_3$ site [46]. Moreover, the C/N atomic ratio rises from 0.823 to 0.855 (Table S2); this proves the incorporation of formamide into g-C_3N_4 frameworks and suggests introducing nitrogen deficiency [47]. The incorporation of N defects may work as trapping centers, considerably reducing the chance of e^--h^+ recombination by capturing the photoinduced electrons and thereby increasing the efficiency of the photocatalytic process [58].

Fig. 2b–e displays the high-resolution C 1s, N 1s, O 1s, and V 2p XPS spectra. Fig. 2b and c illustrate both Ndef-CN and 5VO/Ndef-CN high-resolution spectra, showing similar peaks with a slight change in their locations (~0.05–0.15 eV). The C 1s high-resolution spectrum of Ndef-CN, as displayed in

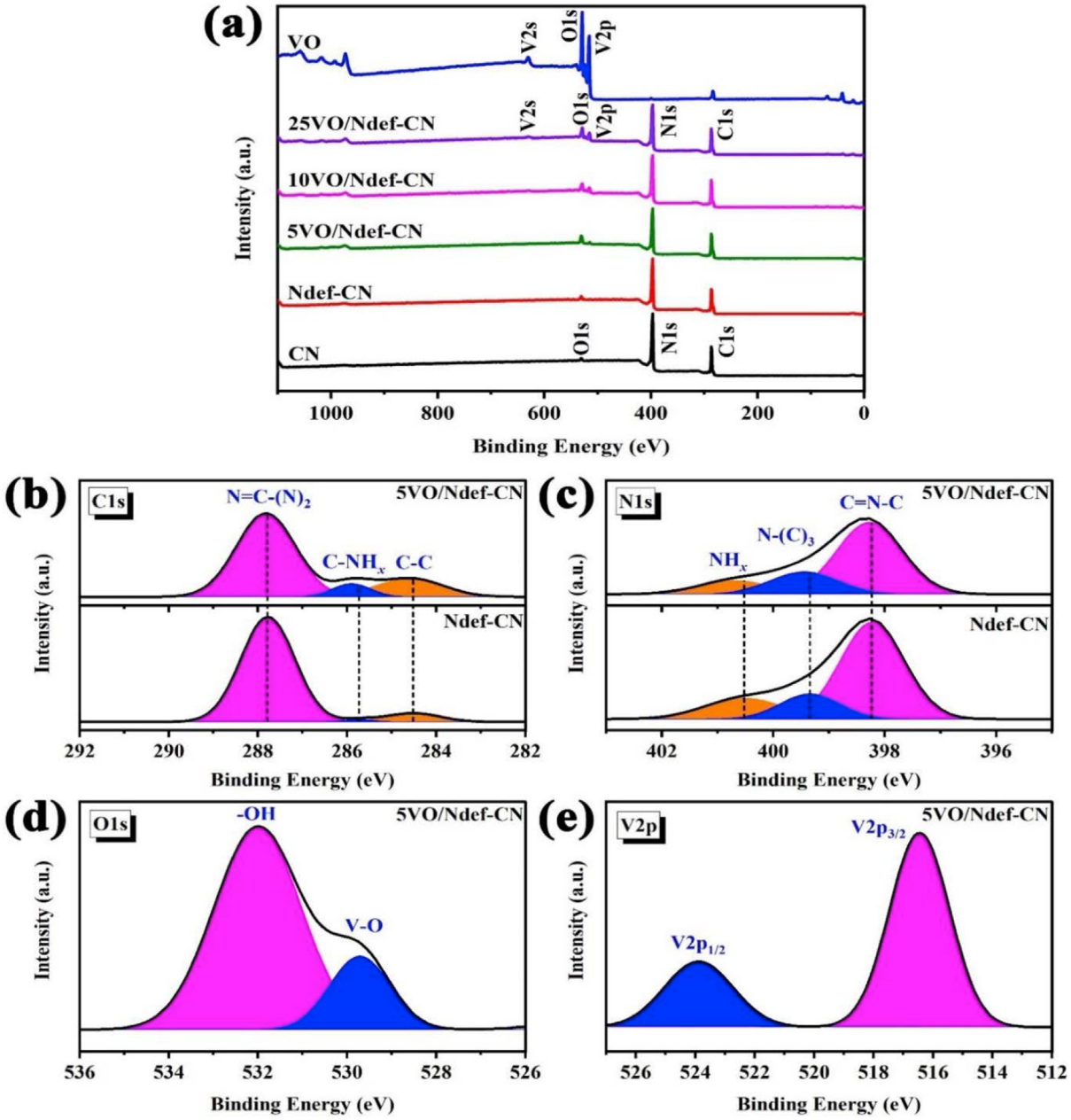

Fig. 2 – (a) XPS survey spectra, (b) C1s and (c) N1s of Ndef-CN and 5VO/Ndef-CN samples, and (d) O1s and (e) V2p of 5VO/Ndef-CN.

Fig. 2b appears to be composed of three Gaussian peaks corresponding to C–C, C-NHx, and the N=C–$(N)_2$ of triazine rings at 284.52, 285.73, and 287.78 eV, respectively [47,58]. In the N 1s spectrum (Fig. 2c), the sp^2-hybridized nitrogen (C=N–C), the inner tertiary nitrogen (N–$(C)_3$) groups, and amino groups (-NH_x) were all observed at 398.23, 399.34, and 400.54 eV, respectively [1,47]. The slight shifts to the higher binding energy of the N 1s and C 1s peaks of 5VO/Ndef-CN may be attributed to the tight contact and interactions between VO and Ndef-CN [2]. The O 1s spectrum of 5VO/Ndef-CN (Fig. 2d) reveals two peaks around 529.71 eV and 532.00 eV, confirming the existence of V–O bonds for the V_2O_5 and OH moiety on the nanocomposite's surface [43,56]. Fig. 2e shows the V 2p high-resolution spectrum, where V $2p_{3/2}$ and V $2p_{1/2}$ have two peaks observed at 516.45 eV and 523.89 eV, respectively, which are ascribed to V^{5+} ions and in agreement with other work [35,43]. The XPS data provided additional evidence that the VO/Ndef-CN heterostructure was successfully constructed.

Morphology analysis

The morphologies of CN, Ndef-CN, and *x*VO/Ndef-CN samples were studied using SEM images. As illustrated in Fig. 3a, pure CN has a stacked thin sheet morphology, whereas the Ndef-CN has similar morphology to CN but slightly curling due to the incorporation of formamide [47]. The pure VO sample exhibits a series of particles with stacked 2D layers and a

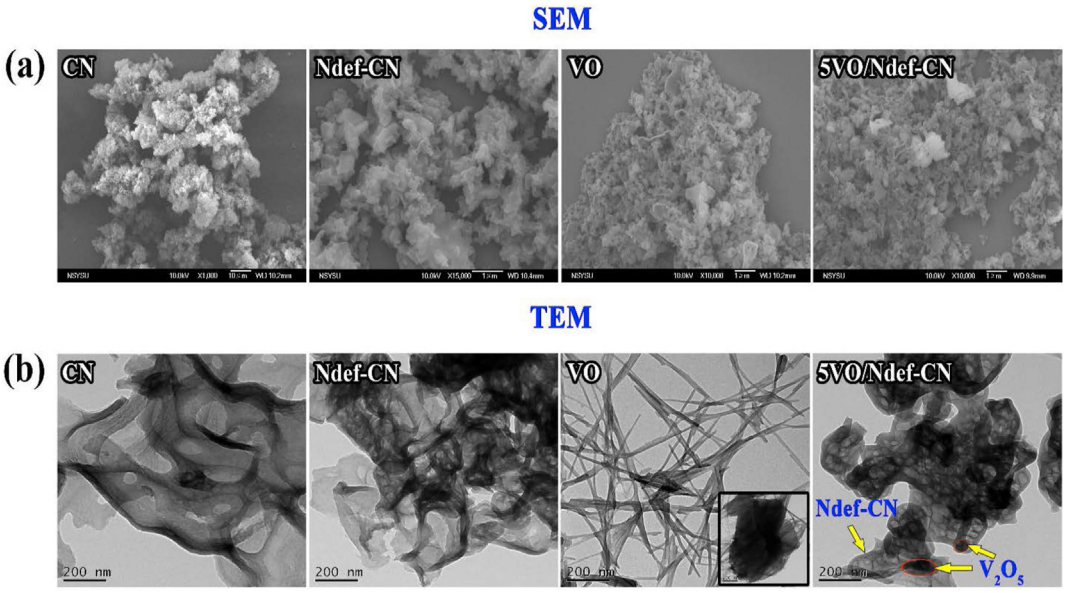

Fig. 3 – (a) SEM images and (b) TEM images of pure CN, Ndef-CN, VO, and 5VO/Ndef-CN samples.

nanoribbon-like structure. After introducing VO, the composite structure shows smaller and highly curled ultrathin nanosheet layers (Fig. 3a and S3a), which can provide a greater number of active sites for the photocatalytic process. Similarly, the Ndef-CN ultrathin nanosheet can act as a unique substrate, preventing VO nanoparticle aggregation [4].

TEM images of the prepared samples are shown in Fig. 3b and S3b. Both CN and Ndef-CN displayed an ultrathin porous nanosheet structure, and Ndef-CN showed more curled edges. On the other hand, several particles with nanoribbon-like morphology were observed in the pure VO sample. As seen in Fig. 3b and S3b, the samples exhibited a layered structure as a result of the addition of VO, with certain agglomerates of VO particles tightly attached and distributed on the 2D Ndef-CN nanosheet surface [1]. The composite exhibited a tightly packed surface morphology, facilitating efficient charge carrier separation. This heterojunction architecture is well known to improve the material's surface area, active sites, and related photocatalytic activity. It can be shown that with the increase of VO weight content, a noticeable agglomeration of VO particles can be observed in the xVO/Ndef-CN composite (Fig. 3b and S3b).

The EDS elemental analysis was performed to elucidate more information about the elemental composition. Fig. S4 illustrates the EDS spectrum of 5VO/Ndef-CN, which contains C, N, V, and O, demonstrating the formation of the 5VO/Ndef-CN heterojunction photocatalytic material.

Optical studies

UV–vis DRS and bandgap analysis

The UV–Vis DRS (Fig. 4a) was measured to investigate the optical properties of CN, Ndef-CN, VO, and xVO/Ndef-CN composites. There is an absorption edge at around 450 nm for pristine CN, whereas Ndef-CN has a remarkable redshift. Therefore, the introduction of the N defect has significantly altered the delocalization of π-electron in the conjugated system of CN [47]. Following the loading of VO, the xVO/Ndef-CN absorbance was greatly enhanced due to the existence of a smaller bandgap semiconductor [53]. The redshift in the xVO/Ndef-CN absorption will improve the photocatalytic performance [43], which may result from the hybrid structure between the Ndef-CN and VO surfaces. The results further demonstrate that all xVO/Ndef-CN photocatalysts are capable of functioning when exposed to visible-light. The Kubelka-Munk equation $(F(R_\infty).h\nu)^{n/2} = A(h\upsilon - E_g)$ gives the corresponding bandgaps of the prepared photocatalysts (Table S1), where ($h\upsilon$) is the photon energy and $F(R_\infty)$ is the Kubelka-Munk function. The n value of VO is 1, and the n value of CN, Ndef-CN, and xVO/Ndef-CN is 4 [1,43]. Thus, the calculated bandgap energies of CN, Ndef-CN, and VO were 2.78, 2.69, and 2.00 eV, respectively (Fig. 4b), which are almost identical to those reported in recent publications [1,47,56,59]. In addition, the bandgaps of 5VO/Ndef-CN, 10VO/Ndef-CN, and 25VO/Ndef-CN were found to be 2.34, 2.28, and 2.23 eV, respectively (Fig. 4b). The narrow bandgap promotes the absorption of visible-light and subsequently enhances the photocatalytic performance. These findings indicate that the bandgap values gradually decreased as the VO content increased in the composite [42].

Photoluminescence analysis

The photogenerated charge separation and transfer efficiency were investigated using PL analysis, in which the photocatalytic activity is inversely proportional to the PL intensity [4]. The PL spectra of the prepared photocatalysts are shown in Fig. 4c. The pure CN shows a broad peak at 456 nm with high emission intensity [1,56] due to e^--h^+ pair recombination. It is evident that introducing the N defect reduces the PL intensity and shifts the emission peak of the Ndef-CN sample to a longer wavelength. The additional electrons at N-deficient sites tend to capture the photogenerated holes, reducing

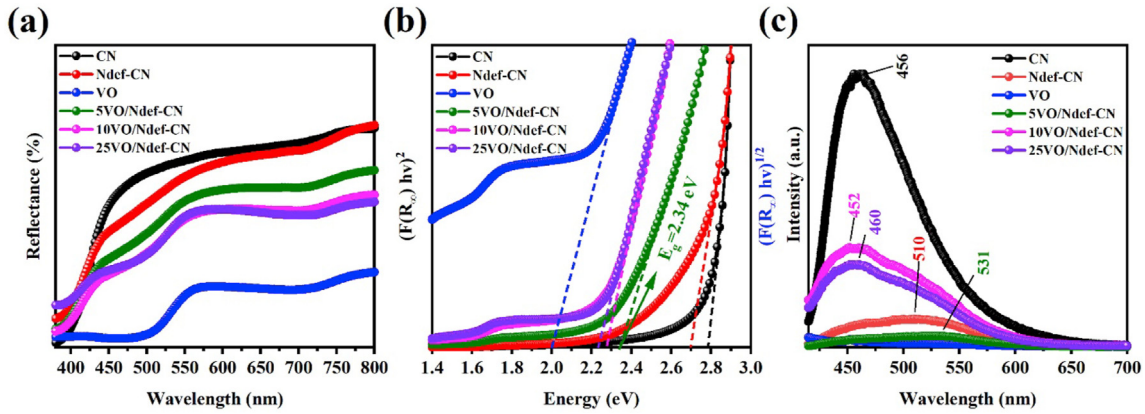

Fig. 4 – (a) UV–Vis DRS, (b) bandgap energies, and (c) PL spectra of pure CN, Ndef-CN, VO, and *x*VO/Ndef-CN samples.

spatial overlap between photoinduced carriers [47]. After loading V_2O_5, the hetero-structured *x*VO/Ndef-CN nanocomposites showed lower PL emission intensity than pure CN [43], which helps to enhance photocatalytic activity. Furthermore, the PL intensity of the 5VO/Ndef-CN possessed the lowest PL intensity, and the emission shifted toward a longer wavelength (531 nm), which is consistent with the narrowing bandgap, suggesting slow electron-hole recombination and indicating its highest photocatalytic activity [4].

Photocatalytic performance

The photocatalytic redox activity of the *x*VO/Ndef-CN nanocomposites was examined for both H_2 generation and pollutant degradation under visible-light irradiation.

Hydrogen generation

The photocatalytic hydrogen generation activity of VO, CN, Ndef-CN, and *x*VO/Ndef-CN nanocomposites was evaluated under visible-light irradiation with and without co-catalyst (Pt) in the presence of TEOA as an electron donor. The H_2 generation without any deposited co-catalyst was about 447 μmol g^{-1} h^{-1}, while the addition of Pt as a co-catalyst increases the H_2 evolution rate (HER), see Fig. S5a. The maximum HER was obtained with a Pt loading of 5% on the catalyst surface (Fig. S5a). Furthermore, the effect of the catalyst dosage on hydrogen production was optimized, as seen in Fig. S5b, and the highest hydrogen generation activity was optimized at 1.5 mg VO/Ndef-CN. In this study, the HER of CN was found to be 451 μmol g^{-1} h^{-1} (Fig. 5b), which is lower than that of the Ndef-CN sample (1811 μmol g^{-1} h^{-1}). This is probably related to the fast recombination of the e^--h^+ pair [2]. After loading VO on the surface of Ndef-CN, the H_2 production activity increases compared to pure-CN. The results illustrated that the VO content greatly influenced the photocatalytic activities of *x*VO/Ndef-CN nanocomposites. Fig. 5b and Table S6 show that the photocatalytic activity improved and reached its maximum at a 5 wt% VO-loaded sample. On the other hand, increasing the VO amount beyond 5 wt% causes a decrease in activity. It might be due to the accumulation of VO on the surface of Ndef-CN, which shields the light absorption [1,60]. The highest hydrogen evolution rate was observed for the 5VO/Ndef-CN (5892 μmol g^{-1} h^{-1}), which was around 13.1 and 147.3 times higher than CN and VO, respectively. This superior performance over 5VO/Ndef-CN might be attributed to efficient charge carriers separation and increased light-harvesting ability induced by the inclusion of formamide in the CN network and constructing a heterojunction with VO [1]. The apparent quantum yield (AQY) results of 5VO/Ndef-CN at different wavelengths are displayed in Fig. 5c. A value of 6.5% AQY was obtained at λ = 420 nm. Surprisingly, 5VO/Ndef-CN shows an AQY of 5.1 and 0.5% at λ = 460 and 500 nm, respectively. Moreover, the catalytic stability of 5VO/Ndef-CN was evaluated by recycling experiments (Fig. 5d). After five cycles, almost no significant change was observed in hydrogen production performance, indicating that the 5VO/Ndef-CN heterostructure is highly stable for H_2 generation.

The most recent developments in g–C_3N_4–based heterojunction photocatalysts for hydrogen evolution are presented in Table S6, indicating that g-C_3N_4 is still an extremely appealing photocatalyst. In light of these results, it is clear that our newly developed 5VO/Ndef-CN photocatalyst possesses a hydrogen evolution rate that is 9, 17, and 12 times higher than that of the recently reported N–MoS_2/S-g-C_3N_4, B-g-C_3N_4/ZnO, and V_2O_5/g-C_3N_4 photocatalysts [1,61,62], which is at the top of the reported photocatalysts (for more details see Table S6). In addition, it has a good AQY compared to the other reported photocatalysts. This improvement is believed to be a result of the well-matched band structure of the S-scheme heterojunction and intimate contact interfaces between V_2O_5 and N-deficient g-C_3N_4.

Pollutants degradation

The photocatalytic performance of *x*VO/Ndef-CN nanocomposites was investigated through IC and AMOX degradation (refer to Fig. 6 and S6). We investigated the photocatalytic performance of the pollutants to identify the perfect composition of photocatalysts that exhibit the maximum photocatalytic efficiency. VO showed the lowest photocatalytic activity, whereas 5VO/Ndef-CN had the maximum efficiency.

For degradation of IC dye, Figs. S6a and c, and Table S7 indicate that the pure VO (5.9%), CN (51.5%), and Ndef-CN (69.1%) samples exhibit low photocatalytic activity. However,

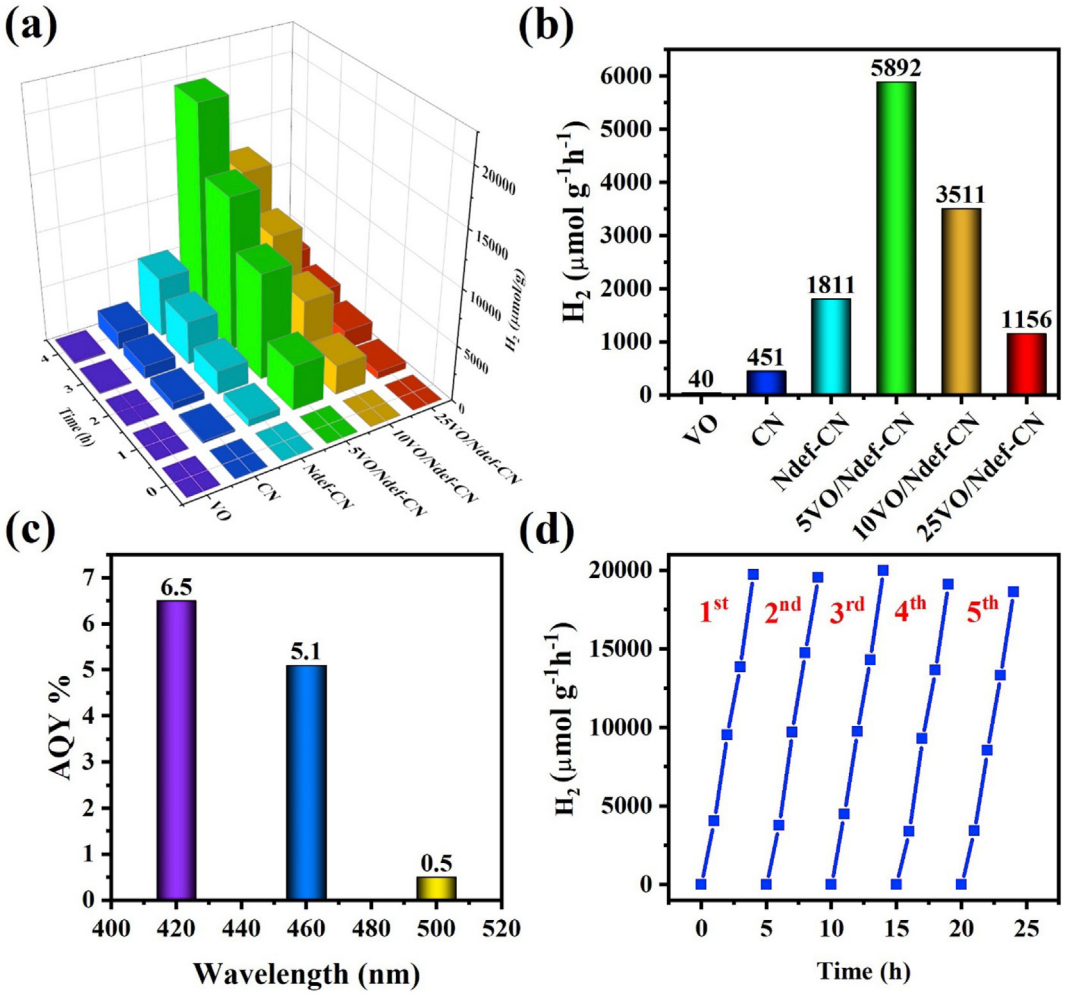

Fig. 5 – (a) H_2 production activity at $\lambda > 420$ nm, and (b) HER with various samples. (c) AQY, and (d) the stability experiment of H_2 evolution over 5VO/Ndef-CN.

the *x*VO/Ndef-CN samples had greater photocatalytic activity than individual photocatalysts (VO, CN, and Ndef-CN). Among all the photocatalysts, the 5VO/Ndef-CN nanocomposite displays the highest photocatalytic activity (98.2%) within 35 min for IC degradation in comparison to other photocatalysts. Besides the dye removal, AMOX was chosen as another representative antibiotic pollutant for further evaluation of the photocatalytic activity. Interestingly, a similar trend has been observed for AMOX "antibiotic" photodegradation (Figs. S6b and d and Table S8); the same composite 5VO/Ndef-CN sample demonstrates the maximum photocatalytic activity of 68.9% in 50 min compared to the observed lower activities for VO (22.0%), CN (28.7%), and Ndef-CN (39.9%) samples. The complete degradation (97.4%) of AMOX over 5VO/Ndef-CN was achieved after 90 min of irradiation, as shown in Fig. S7. The increased photocatalytic performance might be due to better charge carrier separation, a larger SSA, and more active sites. The result illustrates that the VO content significantly influences the photocatalytic activities of *x*VO/Ndef-CN heterostructure photocatalysts. When the VO concentration exceeds 5 wt%, the photocatalytic performance decreases. The reason for decreased performance might be that the excessive VO on the Ndef-CN surface will cover the active site of Ndef-CN and hinder light absorption [4,15].

Fig. 6a, d illustrates the changes in UV–Vis absorption spectra as a function of time for IC and AMOX solutions photodegrading over a 5VO/Ndef-CN catalyst, which is the optimum composition that showed the best performance of 98.2% and 68.9% degradation in 35 min and 50 min, respectively. Fig. 6b,e shows that the C/C_0 ratios for IC and AMOX change over time as a function of all synthesized photocatalysts. The estimated rate constants of the prepared samples are shown in Fig. 6c,f, where the 5VO/Ndef-CN has the most significant rate constant of 0.08185/0.02605 min^{-1} for IC/AMOX, outperforming other photocatalysts (Tables S7 and S8). It can be found that the rate constant for IC degradation over 5VO/Ndef-CN is about 49 times higher, and that for AMOX is found to be about 6 times higher when compared to the activity of pure VO. The total organic carbon (TOC) removal of the degraded pollutants over 5VO/Ndef-CN under visible light irradiation was also evaluated after the degradation process to ensure the mineralization of the pollutants. The experimental results showed that the decay of TOC is about 90% and 57% for IC and AMOX could be achieved after 35 min and 50 min of visible-

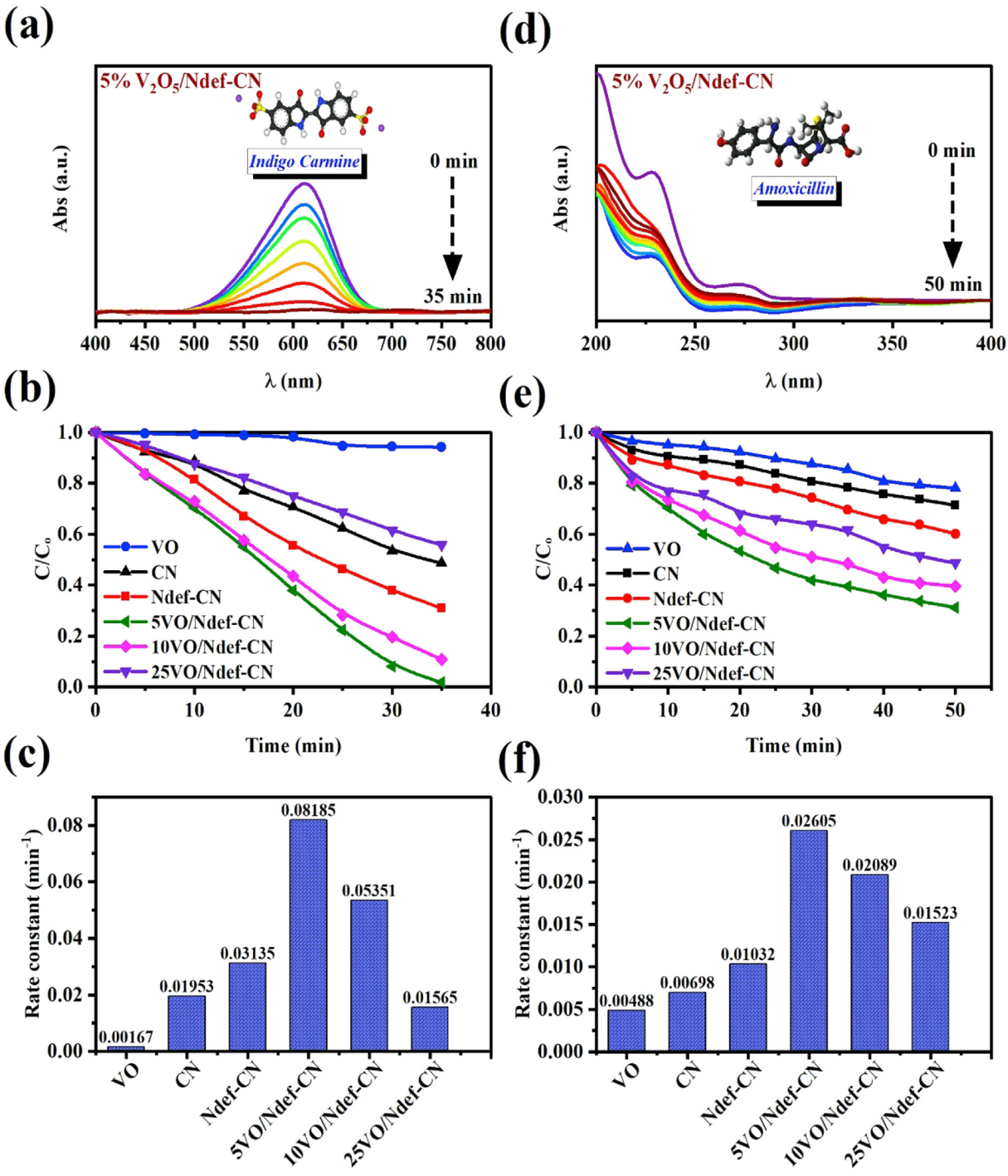

Fig. 6 – (a,d) Changes in IC and AMOX concentrations with time over 5VO/Ndef-CN photocatalyst, respectively, (b,e) Photocatalytic efficiencies for IC and AMOX degradation, and (c,f) The degradation rate constants of IC and AMOX over pure VO, CN, Ndef-CN, and *x*VO/Ndef-CN, respectively.

light irradiation, respectively. According to the TOC experiments, the cleavage of the pollutants chromophore ring structure may be the major process. As a result, these findings show that our photocatalyst exhibits superior efficiency in the degradation (both dyes & antibiotics) and can be a promising candidate for environmental remediation applications. Various photocatalysts have been reported in the literature for the degradation of IC and AMOX; however, the most effective photocatalyst is 5VO/Ndef-CN (Tables S7 and S8). From the results, it can be observed that the degradation efficiency of our photocatalyst (5VO/Ndef-CN) is higher than that of recently published g–C_3N_4–based catalysts for IC degradation, such as ZnO/Bi_2O_3/g-C_3N_4 (93% in 180 min) [63] and g-C_3N_4/MnV_2O_6 (94% in 60 min) [15], besides AMOX degradation, such

as polymeric C_3N_4 (65% in 84 h) [64] and CuO/ZnO@g-C_3N_4 (80% in 120 min) [65]. These photocatalytic degradation results were consistent with those of H_2 evolution studies. The 5VO/Ndef-CN nanocomposite's stability and reusability were investigated using five consecutive recycling experiments in which the 5VO/Ndef-CN was added to the fresh IC solution (Fig. S6e). Even after five cycles, there is no noticeable decrease in the photocatalytic activity, suggesting that our photocatalyst is reasonably stable for multi-use practical applications.

Photocatalytic mechanism and DFT calculations

Radical scavengers test and degradation pathways

We conducted a radical trapping experiment using isopropanol (IPA), *p*-benzoquinone (BQ), and ethylenediaminetetraacetic acid (EDTA), which function as scavengers for ·OH, $O_2^{\bullet-}$, and h^+, respectively, to identify the reactive species formed during the degradation of the IC dye over 5VO/Ndef-CN. When EDTA and BQ were added to the IC solution, the dye degradation was greatly reduced to 54.2% and 78.1%, respectively, whereas IPA had a negligible effect on the IC degradation (Fig. 7a). According to these findings, it is concluded that h^+ and $O_2^{\bullet-}$ play a significant role in IC degradation [59,66].

To elucidate the pollutants' degradation pathways, the electron density, molecular orbitals (HOMO & LUMO), and Fukui Index of IC and AMOX were computed by DFT. Fukui functions were calculated to predict the possible reactive sites. As displayed in Figs. S8a and b, the electron density near the S(1) and C(17) atoms was low for both IC and AMOX, respectively, while the localization of electrons was higher on the other atoms. So, driven by electrostatic attraction, the pollutants were likely to come into contact with the surface of

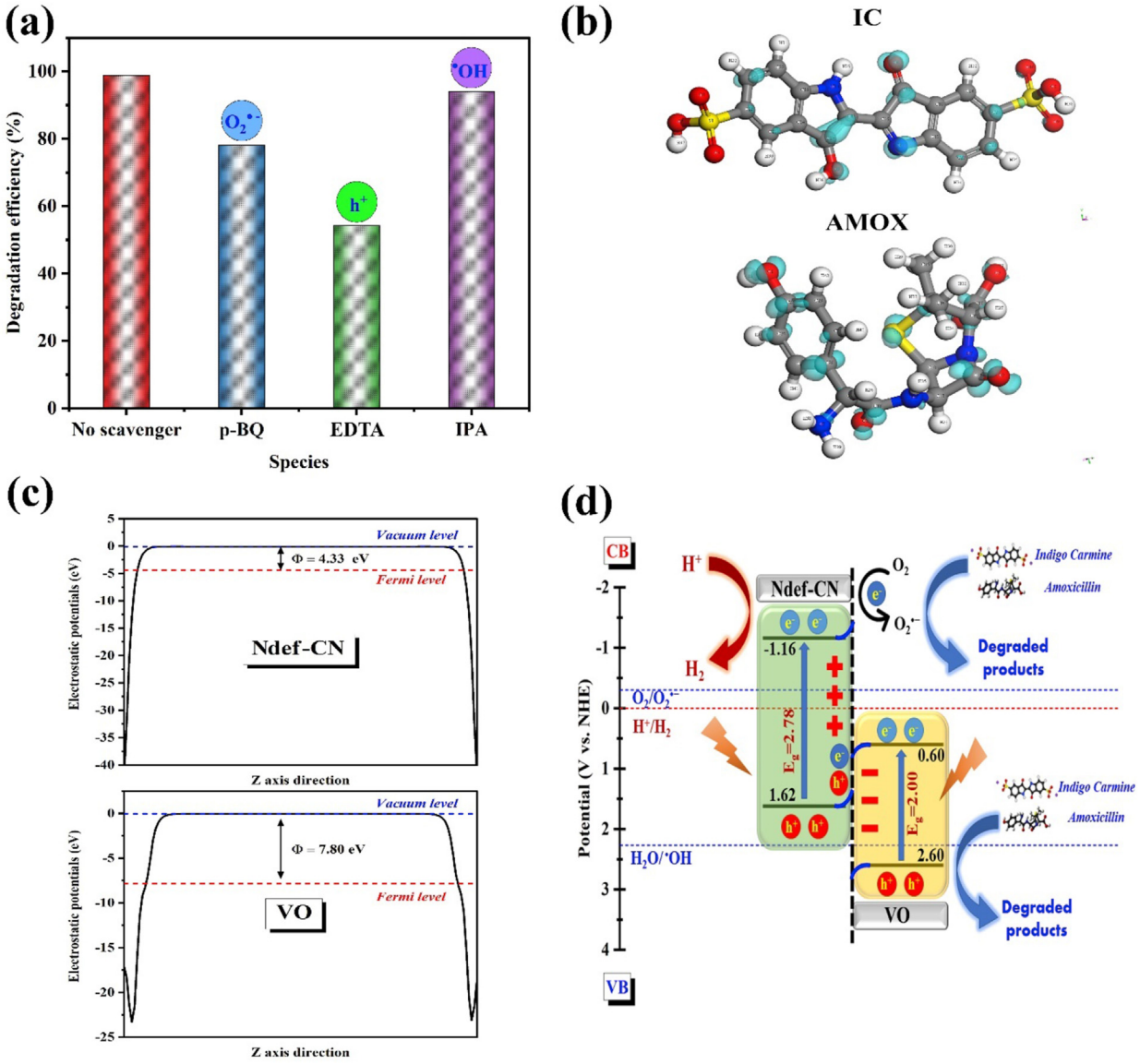

Fig. 7 – (a) The effect of scavengers on the IC degradation over 5VO/Ndef-CN. (b) Isosurface of Fukui index (f^0) distribution on IC and AMOX. (c) Electrostatic potentials of Ndef-CN and VO. (d) Proposed photocatalytic S-scheme mechanism of VO/Ndef-CN nanocomposites for pollutants photodegradation and H_2 production under visible-light irradiation.

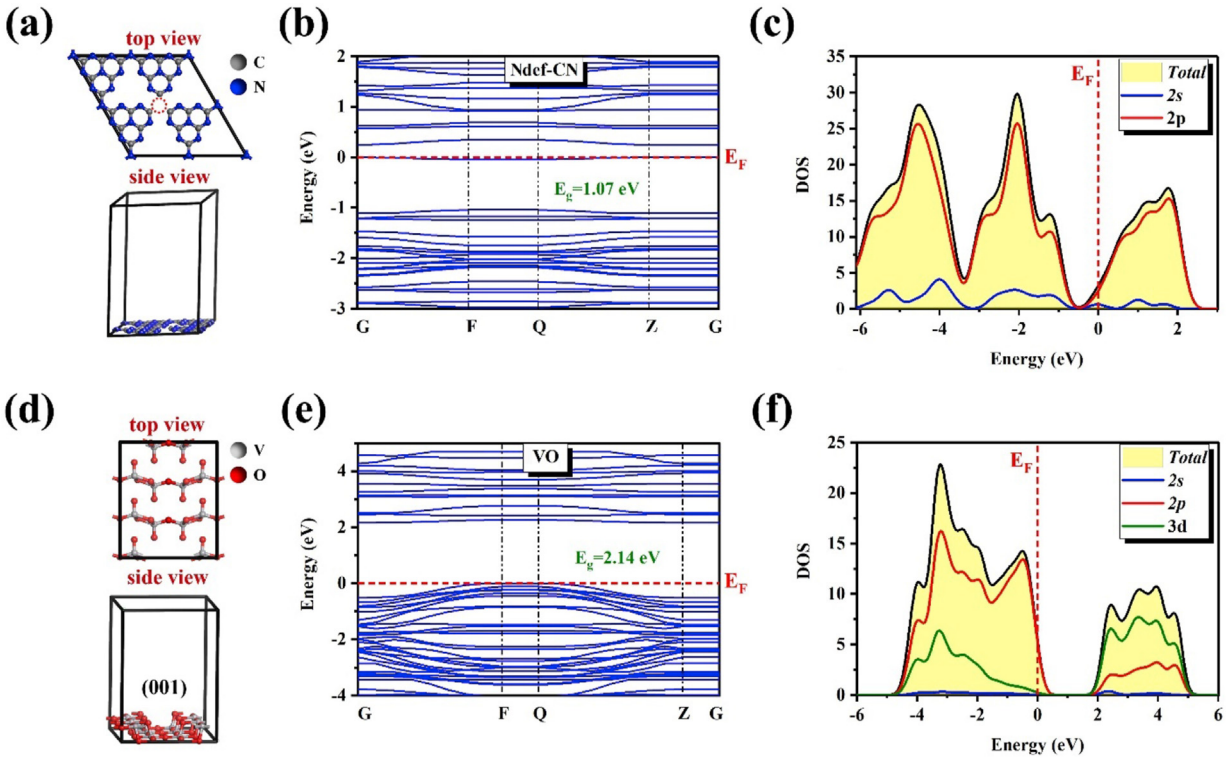

Fig. 8 – (a,d) Optimized crystal structures (top and side views), (b,e) band structures, and (c,f) calculated DOS diagrams of Ndef-CN and VO, respectively.

the photocatalyst. Meanwhile, the HOMO and LUMO orbitals of the IC and AMOX (Figs. S8c and d) are localized over different regions of the molecules, causing molecular stability and preventing self-degradation under normal conditions [4]. In addition, the atoms with larger condensed Fukui index (f^0) values, such as (O3, O4, N12, C17, C20) and (S1, O2, O5, O6, C14) of IC and AMOX, respectively, were suggested to be easily attacked by active species (Fig. 7b and Tables S9 and S10) to form small fragments, which were then mineralized into H_2O and CO_2 [4,67].

Proposed photocatalytic mechanism

In light of the aforementioned experimental findings, the photocatalytic mechanism has been suggested to elucidate the improved performance of the 5VO/Ndef-CN photocatalyst. Fig. 7d shows the separation and transportation of e^--h^+ at the 5VO/Ndef-CN heterojunction interface. The following equations were used to determine the band positions of VO and Ndef-CN photocatalysts:

$$E_{VB} = X - E_e + \frac{1}{2}E_g$$

$$E_{CB} = E_{VB} - E_g$$

where E_{VB}, E_{CB}, X, E_g, and E_e are the valence band, conduction band, semiconductor's electronegativity, optical bandgap values, and free electron energy on the hydrogen scale (~4.5 eV), respectively. While the electronegativity of Ndef-CN and VO are 4.73 and 6.10 eV [35,66]. The calculated CB/VB positions of Ndef-CN and VO are −1.12/1.58 eV and 0.60/2.60 eV, respectively (Fig. 7d). The electronic properties and work function of Ndef-CN and VO were investigated using DFT calculations to better understand the improved photocatalytic activity mechanism of the VO/Ndef-CN nanocomposite. The work function is an important descriptor of the catalyst surface to investigate the charge transfer and determine whether the photocatalytic system is an S-scheme or type II. In this study, the work functions (Φ) of the Ndef-CN and VO (001) surfaces are calculated according to the following equation: $\Phi = E_{vac} - E_F$, where E_{vac} refers to the vacuum level, and E_F is the Fermi energy. As displayed in Fig. 7c, the work functions of the VO (001) surface and monolayer Ndef-CN are 7.80 and 4.33 eV, respectively. Clearly, Ndef-CN has a lower work function than the VO (001) surface. When the VO/Ndef-CN heterostructure is formed, the work function difference between VO and Ndef-CN results in charge rearrangement at the interface, and the electrons will transfer from the surface of Ndef-CN to the VO (001) surface until the Fermi energies of the two systems are equal, which results in band bending in both systems. Moreover, the charge transfer forms an electric field at the interface, which flows from Ndef-CN to VO (001). The electric field helps photogenerated electrons on the CB of VO (001) recombine with the hole on the VB of Ndef-CN, resulting in an increased accumulation of electrons and holes in the CB of Ndef-CN and the VB of VO, respectively (Fig. 7d), which proves that VO/Ndef-CN is an S-scheme heterojunction [19,21].

The holes localized in the VB of VO (2.60 eV) had a significantly larger potential than that in the VB of Ndef-CN (1.58 eV),

and they were capable of directly oxidizing the adsorbed pollutant [59,68]. Due to the Ndef-CN having a lower CB potential (−1.12 eV) than $O_2/O_2^{\bullet-}$ (−0.33 eV), its conduction band electrons reduced the surface oxygen (O_2) to generate superoxide radicals ($O_2^{\bullet-}$), which can oxidize the pollutant owing to their strong oxidative capabilities (Fig. 7d) [59,66]. This finding is in agreement with the results of the radical scavengers' test. The separated electrons on the CB of Ndef-CN (−1.12 eV) are capable of splitting water to generate hydrogen [69]. These electron transfer paths not only improved the efficiency of photogenerated charge carrier transfer and separation, but they also kept the strong redox ability for very efficient photodegradation and H_2 generation.

Electronic properties of Ndef-CN and VO

The electronic structures of Ndef-CN and VO were determined using DFT calculations. Fig. 8a, d illustrate each model's optimized crystal structures (top and side views). Both band structures of the Ndef-CN and VO (001) surfaces (Fig. 8b,e) were calculated using the GGA-PBE method to investigate the enhanced photocatalytic activity of the VO/Ndef-CN heterostructure. It could be found that the Ndef-CN is a direct bandgap semiconductor, and the calculated bandgap (1.07 eV) was decreased by 0.21 eV compared to pure g-C_3N_4 (1.28 eV), indicating that the N deficiency could efficiently narrow the bandgap and improve the photocatalytic activity. Moreover, the VO (001) has a bandgap of 2.14 eV, which agrees well with the observed value (2.00 eV). The total density of states (TDOS) and partial density of states (PDOS) for s, p, and d were calculated to support our results and investigate the orbital contribution(s) of the Ndef-CN and VO systems (Fig. 8c,f). The valence band maximum (VBM) of Ndef-CN is dominated by N the (2p) state, and the conduction band minimum (CBM) is mainly contributed by the C (2p) and N (2p) states, which well reflects the different chemical bonding environments of Ndef-CN. As for VO (001), the DOS analysis indicates that the hybridized states between the V 3d and O 2p orbitals dominate both the VBM and CBM of VO. It is also seen that the contribution of O 2p orbitals is profoundly influencing the VB, while on the CB side, the energy states are contributed mainly by the V 3d orbitals.

Conclusions

In summary, V_2O_5 nanoribbons were successfully coupled with N-deficient g-C_3N_4 through a simple thermal treatment technique to construct new S-scheme photocatalysts (xVO/Ndef-CN). The development of the S-scheme heterojunction enhanced the photoexcited e^--h^+ separation and improved the light-harvesting ability, thus boosting the photocatalytic efficiency, which has been proved by both experimental and theoretical studies. The 5VO/Ndef-CN photocatalyst demonstrated superior photocatalytic performance under visible light for both hydrogen production (5892 μmol g^{-1} h^{-1}) with an AQY of 6.5% at 420 nm and pollutants degradation (98.2% in 35 min and 68.9% in 50 min of IC and AMOX, respectively). In addition, the photocatalyst was found to be stable and reusable, which is essential for its practical applications. It was revealed that $O_2^{\bullet-}$ and h^+ radicals dominate the mechanism of the photodegradation process. This work provides a feasible method to construct a highly effective S-scheme heterojunction photocatalyst for wastewater treatment and clean energy production.

CRediT authorship contribution statement

Ahmed E. Hassan: Conceptualization, Data curation, Formal analysis, Investigation, Methodology, Project administration, Software, Visualization, Writing – original draft, Writing – review & editing. **Mohamed Hammad Elsayed:** Investigation, Methodology, Software, Writing – review & editing. **Mai S. A. Hussien:** Methodology, Resources, Writing – review & editing. **Mohamed Gamal Mohamed:** Investigation, Methodology. **Shiao-Wei Kuo:** Methodology, Writing – review & editing. **Ho-Hsiu Chou:** Methodology, Writing – review & editing. **Ibrahim S. Yahia:** Funding acquisition, Resources, Supervision, Writing – review & editing. **Tarek A. Mohamed:** Software, Validation, Writing – review & editing. **Zhenhai Wen:** Conceptualization, Funding acquisition, Investigation, Project administration, Resources, Supervision, Validation, Writing – review & editing.

Declaration of competing interest

The authors declare that they have no known competing financial interests or personal relationships that could have appeared to influence the work reported in this paper.

Acknowledgments

This research was financially supported by the National Natural Science Foundation of China (Project No. 21875253), CAS-Commonwealth Scientific and Industrial Research Organization (CSIRO) Joint Research Projects (121835KYSB20200039), Scientific Research and Equipment Development Project of CAS (YJKYYQ20190007), Deputyship for Research & Innovation, Ministry of Education, in Saudi Arabia (Project No. IFP-KKU-2020/10), and the CAS-TWAS President's Fellowship for International Doctoral Students. The authors thank the staff at National Sun Yat-Sen University for their assistance with the TEM (ID: EM022600) experiments.

Appendix A. Supplementary data

Supplementary data to this article can be found online at https://doi.org/10.1016/j.ijhydene.2022.12.009.

REFERENCES

[1] Liu B, Yin D, Zhao F, Khaing KK, Chen T, Wu C, et al. Construction of a novel Z-scheme heterojunction with molecular grafted carbon nitride nanosheets and V_2O_5 for highly efficient photocatalysis. J Phys Chem C 2019;123:4193–203.

[2] Shen L, Xing Z, Zou J, Li Z, Wu X, Zhang Y, et al. Black TiO_2 nanobelts/g-C_3N_4 nanosheets laminated heterojunctions with efficient visible-light-driven photocatalytic performance. Sci Rep 2017;7:1–11.

[3] Dadigala R, Bandi R, Gangapuram BR, Dasari A, Belay HH, Guttena V. Fabrication of novel 1D/2D V_2O_5/g-C_3N_4 composites as Z-scheme photocatalysts for CR degradation and Cr(VI) reduction under sunlight irradiation. J Environ Chem Eng 2019;7:102822.

[4] Le S, Zhu C, Cao Y, Wang P, Liu Q, Zhou H, et al. V_2O_5 nanodot-decorated laminar g-C_3N_4 for sustainable photodegradation of amoxicillin under solar light. Appl Catal B Environ 2022;303:120903.

[5] Zhang Y, Zhao J, Wang H, Xiao B, Zhang W, Zhao X, et al. Single-atom Cu anchored catalysts for photocatalytic renewable H_2 production with a quantum efficiency of 56. Nat Commun 2022;13:1–10.

[6] Asadzadeh-Khaneghah S, Habibi-Yangjeh A. g-C_3N_4/carbon dot-based nanocomposites serve as efficacious photocatalysts for environmental purification and energy generation: a review. J Clean Prod 2020;276:124319.

[7] Akhundi A, Badiei A, Ziarani GM, Habibi-Yangjeh A, Munoz-Batista MJ, Luque R. Graphitic carbon nitride-based photocatalysts: toward efficient organic transformation for value-added chemicals production. Mol Catal 2020;488:110902.

[8] Akhundi A, Habibi-Yangjeh A, Abitorabi M, Rahim Pouran S. Review on photocatalytic conversion of carbon dioxide to value-added compounds and renewable fuels by graphitic carbon nitride-based photocatalysts. Catal Rev 2019;61:595–628.

[9] Habibi-Yangjeh A, Asadzadeh-Khaneghah S, Feizpoor S, Rouhi A. Review on heterogeneous photocatalytic disinfection of waterborne, airborne, and foodborne viruses: can we win against pathogenic viruses? J Colloid Interface Sci 2020;580:503–14.

[10] Elsayed MH, Elmorsi TM, Abuelela AM, Hassan AE, Alhakemy AZ, Bakr MF, et al. Direct sunlight-active Na-doped ZnO photocatalyst for the mineralization of organic pollutants at different pH mediums. J Taiwan Inst Chem Eng 2020;115:187–97.

[11] Alhakemy AZ, Senthilkumar N, Ding Y, Li J, Wen Z. Co_3O_4-C@FeMoP on nickel foam as bifunctional electrocatalytic electrode for high-performance alkaline water splitting. Int J Hydrogen Energy 2021;46:32846–57.

[12] Elsayed MH, Abdellah M, Hung Y-H, Jayakumar J, Ting L-Y, Elewa AM, et al. Hydrophobic and hydrophilic conjugated polymer dots as binary photocatalysts for enhanced visible-light-driven hydrogen evolution through förster resonance energy transfer. ACS Appl Mater 2021;13:56554–65.

[13] Li H, Liu Y, Gao X, Fu C, Wang X. Facile synthesis and enhanced visible-light photocatalysis of graphitic carbon nitride composite semiconductors. ChemSusChem 2015;8:1189–96.

[14] Hassan AE, Hussien MS, Elsayed MH, Mohamed MG, Kuo S-W, Chou H-H, et al. One-step construction of Y, C, and O tridoped g-C_3N_4 as a bifunctional photocatalyst for H_2 evolution and organic pollutant degradation under visible light irradiation. Sustain Energy Fuels 2022;6:3858–71.

[15] Nithya M, Vidhya S. A novel g-C_3N_4/MnV_2O_6 heterojunction photocatalyst for the removal of methylene blue and indigo carmine. Chem Phys Lett 2019;737:136832.

[16] Gogoi D, Makkar P, Ghosh NN. Solar light-irradiated photocatalytic degradation of model dyes and industrial dyes by a magnetic $CoFe_2O_4$-g-C_3N_4 S-scheme heterojunction photocatalyst. ACS Omega 2021;6:4831–41.

[17] Kumar A, Sharma SK, Sharma G, Naushad M, Stadler FJ. CeO_2/g-C_3N_4/V_2O_5 ternary nano hetero-structures decorated with CQDs for enhanced photo-reduction capabilities under different light sources: dual Z-scheme mechanism. J Alloys Compd 2020;838:155692.

[18] Sun W, Zhu J, Zheng Y. Graphitic carbon nitride heterojunction photocatalysts for solar hydrogen production. Int J Hydrogen Energy 2021;46:37242–67.

[19] Feng K, Tian J, Hu X, Fan J, Liu E. Active-center-enriched $Ni_{0.85}Se$/g-C_3N_4 S-scheme heterojunction for efficient photocatalytic H_2 generation. Int J Hydrogen Energy 2022;47:4601–13.

[20] Wang F, Hu J, Liang R, Lei W, Lou Z, Pan X, et al. Novel ReS_2/g-C_3N_4 heterojunction photocatalyst formed by electrostatic self-assembly with increased H_2 production. Int J Hydrogen Energy 2022;47:29284–94.

[21] Chen Y, Wang Q, Huang H, Kou J, Lu C, Xu Z. Effective solar driven H_2 production by $Mn_{0.5}Cd_{0.5}Se$/g-C_3N_4 S-scheme heterojunction photocatalysts. Int J Hydrogen Energy 2021;46:32514–22.

[22] Wang J, Wang S. A critical review on graphitic carbon nitride (g-C_3N_4)-based materials: preparation, modification and environmental application. Coord Chem Rev 2022;453:214338.

[23] Hayat A, Al-Sehemi AG, El-Nasser KS, Taha T, Al-Ghamdi AA, Syed JAS, et al. Graphitic carbon nitride (g-C_3N_4)-based semiconductor as a beneficial candidate in photocatalysis diversity. Int J Hydrogen Energy 2021;47:5142–91.

[24] Ajiboye TO, Kuvarega AT, Onwudiwe DC. Graphitic carbon nitride-based catalysts and their applications: a review. Nano-Struct Nano-Objects 2020;24:100577.

[25] Linh PH, Do Chung P, Van Khien N, Thu VT, Bach TN, Hang LT, et al. A simple approach for controlling the morphology of g-C_3N_4 nanosheets with enhanced photocatalytic properties. Diam Relat Mater 2021;111:108214.

[26] Dong Y, Wang D, Zhang H, Chen Y, Liu W, Wang Y. Morphological control of tubular g-C_3N_4 and their visible-light photocatalytic properties. Mater Lett 2017;196:100–3.

[27] Zhu D, Zhou Q. Nitrogen doped g-C_3N_4 with the extremely narrow band gap for excellent photocatalytic activities under visible light. Appl Catal B Environ 2021;281:119474.

[28] Wang S, Zhan J, Chen K, Ali A, Zeng L, Zhao H, et al. Potassium-doped g-C_3N_4 achieving efficient visible-light-driven CO_2 reduction. ACS Sustainable Chem Eng 2020;8:8214–22.

[29] Liu E, Lin X, Hong Y, Yang L, Luo B, Shi W, et al. Rational copolymerization strategy engineered C self-doped g-C_3N_4 for efficient and robust solar photocatalytic H_2 evolution. Renew Energy 2021;178:757–65.

[30] Lin Z, Wang S, Miao Y, Yuan J, Liu Y, Xu S, et al. One-step preparation of halogenated aminobenzonitrile modified g-C_3N_4 via copolymerization and in situ halogen doping for highly enhanced visible light hydrogen evolution. Int J Hydrogen Energy 2020;45:6341–51.

[31] Liang L, Shi L, Wang F, Wang H, Qi W. The improvement of photocatalytic performance for hydrogen evolution over mesoporous g-C_3N_4 modified with nitrogen defects. Sustain Energy Fuels 2020;4:5179–87.

[32] Gao S, Wang X, Song C, Zhou S, Yang F, Kong Y. Engineering carbon-defects on ultrathin g-C_3N_4 allows one-pot output and dramatically boosts photoredox catalytic activity. Appl Catal B Environ 2021;295:120272.

[33] Xu X, Wang J, Shen Y. An interface optimization strategy for g-C_3N_4-based S-scheme heterojunction photocatalysts. Langmuir 2021;37:7254–63.

[34] Preeyanghaa M, Vinesh V, Neppolian B. Construction of S-scheme 1D/2D rod-like g-C_3N_4/V_2O_5 heterostructure with enhanced sonophotocatalytic degradation for Tetracycline antibiotics. Chemosphere 2022;287:132380.

[35] Zhang X, Jia X, Duan P, Xia R, Zhang N, Cheng B, et al. V_2O_5/P-g-C_3N_4 Z-scheme enhanced heterogeneous photocatalytic removal of methyl orange from water under visible light irradiation. Colloids Surf A Physicochem Eng Asp 2021;608:125580.
[36] Du H, Liu Y-N, Shen C-C, Xu A-W. Nanoheterostructured photocatalysts for improving photocatalytic hydrogen production. Chin J Catal 2017;38:1295–306.
[37] Jiang G, Zheng C, Yan T, Jin Z. $Cd_{0.8}Mn_{0.2}S/MoO_3$ composites with an S-scheme heterojunction for efficient photocatalytic hydrogen evolution. Dalton Trans 2021;50:5360–9.
[38] Li Y, Zhou M, Cheng B, Shao Y. Recent advances in g-C_3N_4-based heterojunction photocatalysts. J Mater Sci Technol 2020;56:1–17.
[39] Mishra R, Bera S, Chatterjee R, Banerjee S, Bhattacharya S, Biswas A, et al. A review on Z/S–scheme heterojunction for photocatalytic applications based on metal halide perovskite materials. Appl Surf Sci 2022;9:100241.
[40] Wang L, Bie C, Yu J. Challenges of Z-scheme photocatalytic mechanisms. Trends Chem 2022;4:973–83.
[41] Zhang L, Zhang J, Yu H, Yu J. Emerging S-scheme photocatalyst. Adv Mater 2022;34:2107668.
[42] Wu J, Hua W, Yue Y, Gao Z. Efficient aerobic oxidation of ethyl lactate to ethyl pyruvate over V_2O_5/g-C_3N_4 catalysts. ACS Omega 2020;5:16200–7.
[43] Oliveros AN, Pimentel JAI, de Luna MDG, Garcia-Segura S, Abarca RRM, Doong R-A. Visible-light photocatalytic diclofenac removal by tunable vanadium pentoxide/boron-doped graphitic carbon nitride composite. Chem Eng J 2021;403:126213.
[44] Sun H, Guo F, Pan J, Huang W, Wang K, Shi W. One-pot thermal polymerization route to prepare N-deficient modified g-C_3N_4 for the degradation of tetracycline by the synergistic effect of photocatalysis and persulfate-based advanced oxidation process. Chem Eng J 2021;406:126844.
[45] Wang Y, Zhao S, Zhang Y, Fang J, Chen W, Yuan S, et al. Facile synthesis of self-assembled g-C_3N_4 with abundant nitrogen defects for photocatalytic hydrogen evolution. ACS Sustainable Chem Eng 2018;6:10200–10.
[46] Yu W, Shan X, Zhao Z. Unique nitrogen-deficient carbon nitride homojunction prepared by a facile inserting-removing strategy as an efficient photocatalyst for visible light-driven hydrogen evolution. Appl Catal B Environ 2020;269:118778.
[47] Xu C-Q, Zhang W-D. Facile synthesis of nitrogen deficient g-C_3N_4 by copolymerization of urea and formamide for efficient photocatalytic hydrogen evolution. Mol Catal 2018;453:85–92.
[48] Delley B. From molecules to solids with the DMol3 approach. J Chem Phys 2000;113:7756–64.
[49] Becke AD. Density-functional thermochemistry. III. The role of exact exchange. J Chem Phys 1993;98:5648–52.
[50] Lee C, Yang W, Parr RG. Development of the Colle-Salvetti correlation-energy formula into a functional of the electron density. Phys Rev B 1988;37:785–9.
[51] Perdew JP, Burke K, Ernzerhof M. Generalized gradient approximation made simple. Phys Rev Lett 1996;77:3865.
[52] Zhao S, Zhang Y, Wang Y, Zhou Y, Qiu K, Zhang C, et al. Ionic liquid-assisted synthesis of Br-modified g-C_3N_4 semiconductors with high surface area and highly porous structure for photoredox water splitting. J Power Sources 2017;370:106–13.
[53] Jayaraman T, Raja SA, Priya A, Jagannathan M, Ashokkumar M. Synthesis of a visible-light active V_2O_5-g-C_3N_4 heterojunction as an efficient photocatalytic and photoelectrochemical material. New J Chem 2015;39:1367–74.
[54] Zou H, Xiao G, Chen K, Peng X. Noble metal-free V_2O_5/g-C_3N_4 composites for selective oxidation of olefins using hydrogen peroxide as an oxidant. Dalton Trans 2018;47:13565–72.
[55] Wang Y, Silveri F, Bayazit MK, Ruan Q, Li Y, Xie J, et al. Bandgap engineering of organic semiconductors for highly efficient photocatalytic water splitting. Adv Energy Mater 2018;8:1801084.
[56] Liu Q, Fan C, Tang H, Sun X, Yang J, Cheng X. One-pot synthesis of g-C_3N_4/V_2O_5 composites for visible light-driven photocatalytic activity. Appl Surf Sci 2015;358:188–95.
[57] Wang L, Hou Y, Xiao S, Bi F, Zhao L, Li Y, et al. One-step, high-yield synthesis of g-C_3N_4 nanosheets for enhanced visible light photocatalytic activity. RSC Adv 2019;9:39304–14.
[58] Xiao Y, Tian G, Li W, Xie Y, Jiang B, Tian C, et al. Molecule self-assembly synthesis of porous few-layer carbon nitride for highly efficient photoredox catalysis. J Am Chem Soc 2019;141:2508–15.
[59] Zang Y-N, Yang S-S, Ding J, Zhao S-Y, Chen C-X, He L, et al. A biochar-promoted V_2O_5/g-C_3N_4 Z-Scheme heterostructure for enhanced simulated solar light-driven photocatalytic activity. RSC Adv 2021;11:15106–17.
[60] Han C, Ge L, Chen C, Li Y, Xiao X, Zhang Y, et al. Novel visible light induced Co_3O_4-g-C_3N_4 heterojunction photocatalysts for efficient degradation of methyl orange. Appl Catal B Environ 2014;147:546–53.
[61] Chen Y, Su F, Xie H, Wang R, Ding C, Huang J, et al. One-step construction of S-scheme heterojunctions of N-doped MoS_2 and S-doped g-C_3N_4 for enhanced photocatalytic hydrogen evolution. Chem Eng J 2021;404:126498.
[62] Kim D, Yong K. Boron doping induced charge transfer switching of a g-C_3N_4/ZnO photocatalyst from Z-scheme to type II to enhance photocatalytic hydrogen production. Appl Catal B Environ 2021;282:119538.
[63] Huy BT, Paeng DS, Thao CTB, Phuong NTK, Lee Y-I. ZnO-Bi_2O_3/graphitic carbon nitride photocatalytic system with H_2O_2-assisted enhanced degradation of Indigo carmine under visible light. Arab J Chem 2020;13:3790–800.
[64] Silva IF, Teixeira IF, Rios RD, do Nascimento GM, Binatti I, Victória HF, et al. Amoxicillin photodegradation under visible light catalyzed by metal-free carbon nitride: an investigation of the influence of the structural defects. J Hazard Mater 2021;401:123713.
[65] Moradi M, Hasanvandian F, Isari AA, Hayati F, Kakavandi B, Setayesh SR. CuO and ZnO co-anchored on g-C_3N_4 nanosheets as an affordable double Z-scheme nanocomposite for photocatalytic decontamination of amoxicillin. Appl Catal B Environ 2021;285:119838.
[66] Hong Y, Jiang Y, Li C, Fan W, Yan X, Yan M, et al. In-situ synthesis of direct solid-state Z-scheme V_2O_5/g-C_3N_4 heterojunctions with enhanced visible light efficiency in photocatalytic degradation of pollutants. Appl Catal B Environ 2016;180:663–73.
[67] Ray SK, Dhakal D, Lee SW. Visible light driven Ni-$BaMo_3O_{10}$ photocatalyst for indigo carmine degradation: mechanism and pathways. Mater Sci Semicond Process 2020;105:104697.
[68] Su Q, Li Y, Hu R, Song F, Liu S, Guo C, et al. Heterojunction photocatalysts based on 2D materials: the role of configuration. Adv Sustain Syst 2020;4:2000130.
[69] Vattikuti SP, Reddy PAK, Shim J, Byon C. Synthesis of vanadium-pentoxide-supported graphitic carbon nitride heterostructure and studied their hydrogen evolution activity under solar light. J Mater Sci Mater Electron 2018;29:18760–70.